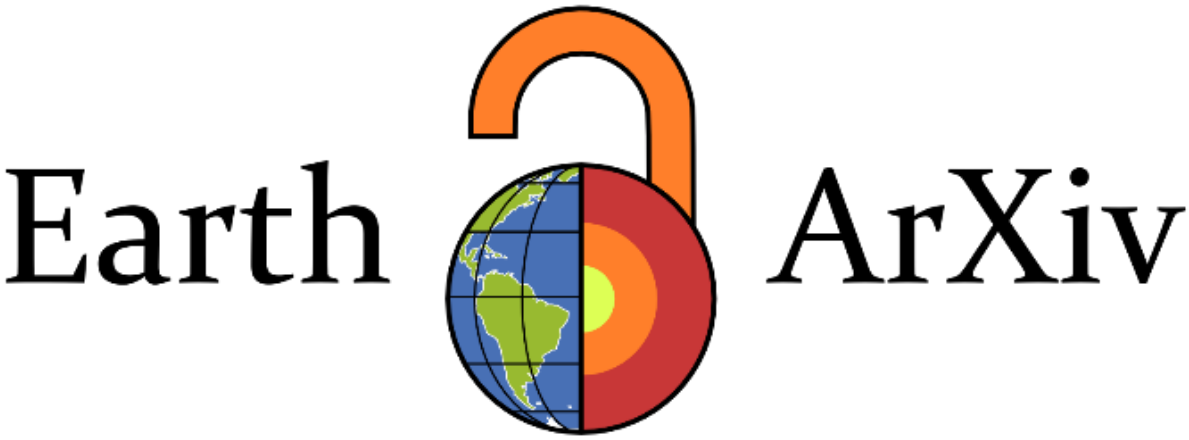

A Fibonacci-Like Propagation Graph for Infiltration and Internal Erosion in Heterogeneous Layered Soils

Simone Cammarasana[†], Marianna Miola[†]
[†]Joint first authors with equal contribution

Istituto di Matematica Applicata e Tecnologie Informatiche
del Consiglio Nazionale delle Ricerche (CNR-IMATI)
Via de Marini 6, 16149, Genova, Italy

simone.cammarasana@cnr.it, marianna.miola@cnr.it

Abstract

Infiltration and internal erosion in heterogeneous layered soils involve coupled flow, pressure build-up, and material degradation across preferential subsurface pathways. High-fidelity Richards-type simulators are physically detailed but can be too expensive for rapid scenario screening and Monte Carlo uncertainty propagation when hydraulic parameters are poorly constrained. We introduce a deterministic reduced-order model in which subsurface pathways are encoded by a *Fibonacci graph* $\mathcal{T}$. The model propagates wetting, pressure, and erosion-propensity indicators through a geotechnically parameterised recurrence, augmented for wetting-front benchmarking by a local reservoir state and an interface-aware hydraulic-contrast correction. Synthetic forcing experiments, uncertainty propagation, and topology ablations show that the Fibonacci graph provides an intermediate-complexity propagation structure between a one-dimensional Chain and a Binary Tree. Direct HYDRUS-1D benchmarks on representative van Genuchten–Mualem homogeneous sand and sand-over-clay profiles show that the interface-aware Fibonacci ROM reproduces the main HYDRUS wetting-front progression with errors on the order of one aggregated depth level. The results support the model as a rapid screening tool for infiltration and pressure-threshold indicators in layered soils.

Keywords: Fibonacci graph, layered soils, infiltration, internal erosion, pressure exceedance, reduced-order model, uncertainty quantification.

1 Introduction

Infiltration and internal erosion in heterogeneous layered soils are governed by complex multiscale interactions between pore-fluid pressure, soil skeleton deformation, and grain transport. These processes are responsible for a wide range of geohazards, slope instability, levee failures, internal piping in earth dams, and shallow landslide initiation, that cause significant

economic losses and loss of life worldwide [Fel07, HLP14]. Classical approaches discretise the governing equations (e.g., Richards equation, dual-porosity models, Biot poroelasticity) on regular grids and solve them numerically [Ric31, Bio41, FO17]. While accurate, these methods are computationally demanding and often require detailed field characterisation that is rarely available in real-case scenarios. Moreover, the strongly nonlinear nature of the Richards equation frequently causes convergence difficulties, especially for infiltration into initially dry or finely textured layered soils [BFRS03, LFOJ23].

The need for reduced-order models A complementary direction is the development of *reduced-order models* (ROMs) that capture the essential physics with a reduced mathematical structure [QMN15, BGW15]. ROMs are particularly valuable in uncertainty quantification (UQ) workflows, where thousands of forward simulations are needed to propagate geotechnical parameter uncertainty to hazard metrics [TPTG17]. The challenge is to design a ROM that is (i) physically interpretable, so that its parameters are directly tied to measurable soil properties; (ii) sufficiently flexible to represent heterogeneous, layered media; and (iii) computationally cheap to enable Monte Carlo propagation. Existing ROMs for subsurface flow typically reduce a pre-existing high-fidelity *partial differential equation* (PDE) solver via projection or interpolation [NKE19, PGP14]; they therefore inherit the mesh and the governing equations of the full model, which limits their parameter-space agility. Our work applies a different approach: we posit a structurally novel, recurrence-based model from the outset, without any underlying PDE solver.

Branching topology of subsurface pathways We propose such a model, based on the observation that subsurface propagation is inherently *branching*: as water or an erosion front descends through a heterogeneous medium, it splits into preferential pathways whose number and connectivity change with depth. This branching character has been well documented at both the pore scale and the continuum scale [TZBL21, ZLEB21, KPRAM23]. Graph-theoretic representations of porous media have been used to identify preferential flow paths [TZBL21, KPRAM23] and to serve as backbones for graph neural network surrogates of fractured-media flow [Jia24], but a simple, closed-form branching model with analytically tractable recurrence structure has not been proposed for geo-hydraulic propagation.

The Fibonacci graph We formalise the branching structure as a Fibonacci graph $\mathcal{T} = (V, E, W)$, where the number of nodes at each depth level follows the Fibonacci sequence. This choice is motivated by structural economy and analytical tractability rather than by a claim that soils are intrinsically Fibonacci: the Fibonacci graph is a simple deterministic, aperiodic branching structure that grows super-linearly with depth, placing it in a distinct class from both periodic lattices, where all paths are topologically equivalent, and fully random percolation graphs, where analytical control is limited [Sah94]. The golden-ratio growth rate produces a moderate branching fan that avoids the combinatorial explosion of a binary tree while still capturing the progressive splitting of preferential pathways as water descends through a heterogeneous medium.

The recurrence connecting a node to its two ancestors naturally encodes both short-memory inheritance from level $n-1$ and long-memory inheritance from level $n-2$, a feature

absent from standard lattice models. In the proposed ROM, this graph is not used only as a geometric scaffold: each node carries soil properties, including porosity, hydraulic conductivity, and pressure threshold, and these properties modulate the local propagation coefficients. The resulting dynamics separate a transient pressure-like signal from a persistent wetting-storage state, allowing the model to retain the computational simplicity of a feed-forward recurrence while representing the cumulative nature of wetting-front advance. For layered profiles, an interface-aware correction based on hydraulic-conductivity contrast further modulates transfer between adjacent levels, so that the same Fibonacci topology can represent both homogeneous and stratified benchmark cases.

To the best of our knowledge, this specific combination of a Fibonacci-like propagation graph, geotechnically parameterised recurrence, local wetting storage, and interface-aware hydraulic-contrast correction has not been previously explored for reduced-order geo-hydraulic modelling (Sect. 2).

Benchmarking strategy We evaluate the model at three complementary levels. First, synthetic root forcings (impulse, step, ramp, sinusoid, and Gaussian) are used to expose the internal propagation regimes of the recurrence and the associated pressure-threshold indicators. Second, Monte Carlo perturbations of porosity and hydraulic conductivity quantify the sensitivity of the output metrics to coefficient-level geotechnical uncertainty, while a Chain/Binary/Fibonacci ablation isolates the role of graph topology at equal depth. Third, to connect the reduced-order dynamics with a standard physically based simulator, the interface-aware reservoir version of the Fibonacci ROM is benchmarked directly against HYDRUS-1D on representative homogeneous sand and sand-over-clay van Genuchten–Mualem profiles under the same Gaussian storm forcing. The numerical workflow is designed to remain reproducible, following recent work on lightweight persistence of geoscientific pipelines [MCP+26].

Contributions This paper makes the following contributions.

(i) We introduce a Fibonacci geo-hydraulic graph and a geotechnically weighted recurrence for wetting, pressure, and erosion-propensity propagation (Sects. 3–4).

(ii) We augment the wetting component with an interface-aware reservoir update and define pressure-threshold indicators for rapid screening in heterogeneous layered soils (Sect. 4).

(iii) We evaluate the model under canonical surface forcings, Monte Carlo parameter perturbations, and geomorphological visualisation of the propagation front (Sect. 5).

(iv) We benchmark the interface-aware reservoir ROM directly against HYDRUS-1D on representative homogeneous and layered van Genuchten–Mualem profiles (Sect. 6).

(v) We analyse the role of topology through a Chain/Binary/Fibonacci ablation and discuss the resulting complexity–descriptive-capacity trade-off (Sect. 7).

Our methodology is implemented in a source code publicly available at the following Github repository: `https://github.com/mariannamiola/geoFib`.

2 Related Work

Infiltration and unsaturated flow The modelling of water movement in unsaturated soils is dominated by the Richards equation [Ric31], which combines Darcy's law [Dar56] with a mass-conservation statement and nonlinear constitutive relations for hydraulic conductivity and capillary pressure. Numerical solution of the Richards equation is challenging due to its strongly nonlinear coefficients, the occurrence of sharp wetting fronts, and possible degeneracy near full saturation or complete dryness. In [FO17], the authors survey finite difference, finite element, and finite volume approaches, highlighting persistent difficulties with mass balance and convergence in layered soils. In [BFRS03], the authors provide a systematic numerical comparison for layered profiles, confirming that the choice of interlayer conductivity algorithm critically affects accuracy. HYDRUS-1D is a widely used one-dimensional implementation of Richards-equation modelling for variably saturated flow, and has been adopted extensively for flow and transport simulations in soils [vvGv08].

Alternative parsimonious infiltration models have been developed to reduce computational cost while retaining physical realism. The Green-Ampt approach and its extensions to layered soils provide closed-form estimates of infiltration depth [LFOJ23]. Dual-porosity models [GVG93] account for preferential flow through macropores and the soil matrix, introducing a source-sink exchange term but at the cost of additional parameters. Physics-informed neural networks have recently been applied to the Richards equation, offering a data-driven route to fast approximation while satisfying the governing PDE as a soft constraint [LSFW25]. Our Fibonacci graph ROM occupies a complementary niche: it is fully deterministic, parameter-lean, and analytically tractable, making it suitable for rapid hazard screening rather than high-fidelity site-specific prediction.

Internal erosion and piping Internal erosion, the detachment and transport of soil particles by seeping water, is the second most common cause of failure in levees and one of the leading causes of failure in earth dams [FF07]. In [Fel07], the authors describe four phases: initiation, continuation, progression to form a pipe, and breach, with pore-pressure exceedance of a critical threshold governing the transition from initiation to progression. Experimental and field evidence confirms that this threshold is strongly dependent on soil gradation, hydraulic conductivity, and confinement stress [LSC+25, LTL24].

Numerical models of internal erosion range from continuum approaches, in which erosion is represented as a source term in the mass-balance equation, to discrete particle methods that resolve grain-scale interactions [Tao18]. The pore-pressure threshold used in the present model is consistent with the hydraulic criterion used in practice and reviewed in [LSC+25].

Preferential flow and graph-based representations Flow in heterogeneous porous media is often concentrated on distinct preferential pathways [ZLEB21, TZBL21]. The emergence and quantification of preferential paths has been studied using random walk particle tracking [PBBK08], entropy-based frameworks [ZLEB21], and graph-theoretic minimum-resistance formulations [KPRAM23]. In [TZBL21], the authors use pore-network graphs to identify conditions under which flow concentration transitions from diffuse to channelled. Our Fibonacci graph formalises a related but distinct idea: rather than inferring the topology from

a flow simulation, we prescribe a branching topology a priori and study how geo-hydraulic state propagates through it.

Graph neural networks (GNNs) have recently been applied as surrogates for subsurface flow in fractured media [Jia24], demonstrating that graph-structured representations can capture the effect of connectivity on pressure and saturation fields. Our model is a stand-alone ROM whose graph structure is fixed and whose dynamics are governed by a closed-form recurrence, making it complementary to GNN-based approaches.

Reduced-order models and uncertainty quantification Reduced-order modelling of subsurface flow has been pursued through proper orthogonal decomposition [NKE19], multiscale finite volume methods [DC12], and greedy algorithms for stochastic groundwater flow [PGP14]. These methods accelerate the solution of full PDE models but still require an underlying high-fidelity solver. The Fibonacci ROM does not reduce an existing solver; it posits a structurally different, recurrence-based model from the outset.

For uncertainty quantification, Monte Carlo simulation remains the most robust approach despite slow convergence [TPTG17]. Geotechnical parameters such as porosity and hydraulic conductivity are well known to span several orders of magnitude and to follow approximately log-normal distributions, as documented in global datasets such as SoilGrids [PDSB+21] and GSHP [GPL+22]. Our model accommodates this uncertainty natively: Monte Carlo realisations are generated by drawing from the parameter distributions defined in Sect. 4 and re-running the cheap recurrence, typically in milliseconds per realisation.

Poroelastic and coupled models The full coupling between fluid flow and solid deformation is described by Biot's theory of consolidation [Bio41], which has been extended to layered soils and unsaturated media [LSC14], and to probabilistic settings [DYCW22]. Poroelastic models are physically rich but require the solution of a coupled PDE system that is even more expensive than the Richards equation alone. Our model decouples fluid propagation from skeleton deformation, retaining only an erosion-propensity proxy for mechanical degradation; full poroelastic coupling is identified as a natural direction for future work.

3 The Fibonacci Propagation Graph

We define the discrete propagation architecture used throughout the paper. The goal is not to claim that natural soils follow an exact Fibonacci geometry, but to introduce a deterministic, moderately branching graph that can represent depth-dependent splitting of preferential pathways while remaining analytically tractable.

3.1 Graph construction

Definition 3.1 (Fibonacci sequence)**.** *The Fibonacci sequence* $\{F_n\}_{n\geq 1}$ *is defined by* $F_1 = F_2 = 1$ *and* $F_n = F_{n-1} + F_{n-2}$ *for* $n \geq 3$*.*

Definition 3.2 (Fibonacci geo-hydraulic graph)**.** *The* Fibonacci geo-hydraulic graph *is a directed acyclic graph* $\mathcal{T} = (V, E, W)$ *constructed as follows.*

(i) ***Levels.*** *The node set V is partitioned into L levels $V = V_0 \cup V_1 \cup \cdots \cup V_{L-1}$, where $|V_k| = F_{k+1}$ for $k = 0, 1, \ldots, L-1$. Level $k = 0$ consists of a single* root *node v_0, representing the soil surface.*

(ii) ***Edges.*** *Every node $v \in V_k$ with $k \geq 1$ has exactly two parents:*

- *a* primary parent $p_1(v) \in V_{k-1}$ *(Fibonacci memory $n-1$);*
- *a* secondary parent $p_2(v) \in V_{k-2}$ *(Fibonacci memory $n-2$, defined for $k \geq 2$).*

For $k = 1$ only the primary parent exists (formally $p_2(v)$ is undefined and the β_v term is dropped). Denoting the j-th node at level k as $v_{k,j}$ (with $j = 1, \ldots, F_{k+1}$), the parent mapping is defined by the following rule:

$$p_1(v_{k,j}) = v_{k-1,\,\lceil j \cdot F_k / F_{k+1} \rceil}, \tag{1}$$

$$p_2(v_{k,j}) = v_{k-2,\,\lceil j \cdot F_{k-1} / F_{k+1} \rceil}, \quad k \geq 2. \tag{2}$$

This proportional index mapping *distributes children approximately uniformly across parents at each level. The primary parent mapping has maximum fan-out bounded by $\lceil F_{k+1}/F_k \rceil \leq 2$. The secondary parent mapping can have fan-out up to 3, and the total outgoing degree of a node can therefore exceed 2; in the $L = 7$ implementation used below, the observed maximum total outgoing degree is 5.*

(iii) ***Edge weights.*** *Each edge $(u, v) \in E$ carries a weight $w_{u \to v} \in \mathbb{R}_{>0}$ defined by the geotechnical properties of the endpoint nodes (Sect. 3.3).*

The total number of nodes is $\sum_{k=0}^{L-1} F_{k+1} = F_{L+2} - 1$.

Remark 3.3. *The Fibonacci graph is neither periodic (as a regular lattice would be) nor random (as a percolation cluster). It is* deterministic *and* aperiodic*, growing with the golden ratio $\varphi = (1+\sqrt{5})/2$ per level. This places it in a structurally distinct class from both periodic lattices and random graphs: it is more flexible than a lattice (no two levels are identical) yet fully analytically tractable, unlike a random topology.*

3.2 Node properties

Each node $v \in V_k$ is characterised by a vector of geotechnical properties:

$$\mathbf{g}_v = \big(\phi_v,\ \kappa_v,\ E_v,\ \tau_{c,v}\big), \tag{3}$$

where $\phi_v \in (0, 1)$ is the *porosity*; $\kappa_v > 0$ is the *saturated hydraulic conductivity* [$\mathrm{m\,s^{-1}}$]; $E_v > 0$ is the *drained stiffness modulus* [MPa] (reserved for future poroelastic coupling); and $\tau_{c,v} > 0$ is the *erosion pressure threshold*.

3.3 Edge weights

The weight on the edge (u, v) models the effective hydraulic transmissivity between the two soil zones. We adopt the *harmonic mean* of the hydraulic conductivities, which is physically motivated by Darcy's law for flow in series through two layers of equal thickness [Dar56]:

$$w_{u\to v} = \frac{2\,\kappa_u\,\kappa_v}{\kappa_u + \kappa_v}. \tag{4}$$

This ensures that the unnormalised weight is dominated by the less permeable node, consistent with the physical principle that the least permeable layer controls the overall flux. In the recurrence below, however, these weights are normalised across the available parents. They therefore encode the relative partition of incoming signal between ancestral paths, not an absolute hydraulic barrier effect. Consequently, multiplying all hydraulic conductivities by a common factor leaves the normalised weights unchanged. Absolute conductivity losses are therefore not represented by the normalised weights themselves, but only indirectly through the recurrence coefficients.

4 Geo-Hydraulic Dynamics

We describe the reduced-order dynamics assigned to the graph. The model propagates dimensionless wetting and pressure signals through the feed-forward topology and uses threshold-based indicators to identify nodes where pressure exceedance occurs. For comparison with Richards-equation simulations, we use an interface-aware reservoir instantiation of the same Fibonacci graph: the pressure-like component remains a transient propagated signal, while the wetting component is updated as a local storage variable that can retain water between time steps. This extension preserves the graph topology and the geotechnical coefficient map, but makes the wetting-front metric closer to the persistent water-content response produced by Richards-type models.

4.1 State variables and Fibonacci recurrence

At each node $v \in V$ and discrete time step $t \in \{0, 1, \ldots, T\}$, the geo-hydraulic state is described by

$$\mathbf{x}_v^{(t)} = \left(\theta_v^{(t)},\ p_v^{(t)},\ e_v^{(t)}\right) \in \mathbb{R}^3, \tag{5}$$

where $\theta_v^{(t)} \geq 0$ is a dimensionless *wetting signal* or, in the reservoir instantiation, a local wetting-storage state, $p_v^{(t)} \geq 0$ is the *normalised pore pressure*, and $e_v^{(t)} \geq 0$ is an instantaneous *erosion-propensity proxy*. We do not interpret $\theta_v^{(t)}$ as a calibrated volumetric water content bounded by one, because the synthetic root forcings may have amplitudes larger than one.

The evolution at node $v \in V_k$ $(k \geq 1)$ follows the *Fibonacci-like recurrence with geotechnical weights*:

$$\mathbf{x}_v^{(t+1)} = \alpha_v \odot \tilde{w}_1(v)\,\mathbf{x}_{p_1(v)}^{(t)} \ +\ \beta_v \odot \tilde{w}_2(v)\,\mathbf{x}_{p_2(v)}^{(t)} \ +\ \mathbf{f}_v^{(t)}, \tag{6}$$

where $\odot$ is the componentwise product, $\tilde{w}_1(v)$ and $\tilde{w}_2(v)$ are normalised edge weights defined by

$$\tilde{w}_1(v) = \frac{w_{p_1(v)\to v}}{w_{p_1(v)\to v} + w_{p_2(v)\to v}}, \qquad \tilde{w}_2(v) = 1 - \tilde{w}_1(v), \tag{7}$$

so that $\tilde{w}_1(v)+\tilde{w}_2(v)=1$ and both weights are non-negative. For nodes at level $k=1$, which have only a primary parent, we set $\tilde{w}_1(v)=1$ and $\tilde{w}_2(v)=0$ by convention. $\mathbf{f}_v^{(t)}$ is an external forcing term (zero for all nodes except the root), and $\alpha_v=(\alpha_v^\theta,\alpha_v^p,\alpha_v^e)$, $\beta_v=(\beta_v^\theta,\beta_v^p,\beta_v^e)$ are the recurrence coefficient vectors.

Remark 4.1 (Relation to the classical Fibonacci recurrence)**.** *When all nodes have identical properties and the two incoming edge weights are equal, equation (6) reduces, after absorbing the normalised weights into the coefficients, to a scalar Fibonacci-like recurrence of the form $x_n = ax_{n-1} + bx_{n-2} + f$. Its spectral properties and asymptotic behaviour are related to the classical theory of linear recurrences [Leh30, KM03]. The graph generalisation introduces spatial heterogeneity and branching.*

Interface-aware reservoir wetting update For wetting-front comparisons with HYDRUS-1D, the wetting component is updated through a local reservoir law. Let

$$g_{u\to v}=\left(\frac{w_{u\to v}}{w_{u\to v}+\kappa_{50}}\right)^{\gamma} \tag{8}$$

be an absolute-conductivity transmission factor, where $\kappa_{50}>0$ sets the conductivity scale at which transmission is half-effective and $\gamma>0$ controls the sharpness of the transition. To account for hydraulic contrasts at layer interfaces, define

$$R_{u,v}=\left|\log_{10}\left(\frac{\kappa_v}{\kappa_u}\right)\right|, \qquad \chi_{u,v}=1+s_I\,\max\{0,R_{u,v}-R_0\}, \tag{9}$$

where R_0 is a contrast threshold and $s_I\geq 0$ is an interface-strength parameter. The reservoir input at node v is

$$I_v^{(t)}=\sum_{i\in\{1,2\}}\tilde{w}_i(v)\,g_{p_i(v)\to v}\,\chi_{p_i(v),v}\,\theta_{p_i(v)}^{(t)}, \tag{10}$$

with the secondary term omitted when $p_2(v)$ is undefined. The wetting state is then advanced by

$$\theta_v^{(t+1)}=\Pi_{[0,1]}\left((1-\delta_v)\theta_v^{(t)}+\frac{\Delta t}{T_v}I_v^{(t)}\right), \tag{11}$$

where $g_v=\sum_{i\in\{1,2\}}\tilde{w}_i(v)g_{p_i(v)\to v}$ is the parent-weighted conductivity transmission, $T_v=T_{\min}+T_{\text{scale}}(1-g_v)$ is an effective filling time, $\delta_v=\Delta t/T_{\text{drain}}$ is a drainage fraction, and $\Pi_{[0,1]}$ denotes the projection onto the admissible wetting interval, $\Pi_{[0,1]}(y)=\min\{1,\max\{0,y\}\}$. The parameters κ_{50}, γ, s_I, R_0, $T_{\min}$, T_{scale}, and T_{drain} are modelling parameters specified in the experimental setup.

4.2 Recurrence coefficients from geotechnical properties

The coefficients α_v and β_v are parameterised from (ϕ_v,κ_v) via the following heuristic map. Let κ_v^{norm} be the log-normalised conductivity in $[0,1]$, and define the *base propagation coefficient*:

$$b_v=\min\{b_{\max},\max\{b_{\min},c_0+c_\kappa\,\kappa_v^{\text{norm}}\,(1-c_\phi\,\phi_v)\}\}. \tag{12}$$

Here c_0 is the baseline propagation level, c_κ controls the conductivity-driven increase in propagation, c_ϕ controls the damping associated with porosity/storage effects, and $b_{\min}$ and $b_{\max}$ set lower and upper bounds for the base coefficient. High κ_v therefore increases b_v (faster propagation), while high ϕ_v decreases b_v (more storage, slower propagation). The componentwise coefficients are then written as $\alpha_v = b_v\,\boldsymbol{\eta}_\alpha$ and $\beta_v = b_v\,\boldsymbol{\eta}_\beta$, where $\boldsymbol{\eta}_\alpha \in \mathbb{R}^3_+$ and $\boldsymbol{\eta}_\beta \in \mathbb{R}^3_+$ are component weights for the wetting, pressure, and erosion-propensity components. The vector $\boldsymbol{\eta}_\alpha$ controls the primary-parent contribution, whereas $\boldsymbol{\eta}_\beta$ controls the secondary-memory contribution. In the experiments we choose $\boldsymbol{\eta}_\beta$ componentwise smaller than $\boldsymbol{\eta}_\alpha$ to encode a weaker influence of the longer-range $n-2$ memory term. A rescaling is enforced, when needed, to keep $\alpha_v^c + \beta_v^c < 1$ for each component c. The numerical instantiation of these parameters is reported in Sect. 5.

Proposition 4.2 (Finite-time zero-input extinction of the feed-forward component)**.** *Assume that the graph has L finite levels and that the root forcing satisfies $\mathbf{x}_{v_0}^{(t)} = \mathbf{0}$ for all $t \geq t_0$. For the purely feed-forward recurrence in equation (6), every node $v \in V_k$ satisfies $\mathbf{x}_v^{(t)} = \mathbf{0}$ for all $t \geq t_0 + k$. In particular, the whole feed-forward response is zero for all $t \geq t_0 + L - 1$. When the reservoir update is used for θ_v, this finite-time extinction property applies to the transient propagated component, while the reservoir state remains bounded in $[0, 1]$ and decays according to the drainage term.*

Proof. The root case $k = 0$ follows directly from the assumption. Suppose the claim holds for all nodes up to level $k-1$. A node $v \in V_k$ depends only on its parents in levels $k-1$ and, when present, $k-2$ at the previous time step; there is no self-memory term involving $\mathbf{x}_v^{(t)}$. Hence, once all parent states are zero, equation (6) gives $\mathbf{x}_v^{(t+1)} = 0$. Induction over the finite depth of the directed acyclic graph proves the claim. □

Remark 4.3. *The condition $\alpha_v^c + \beta_v^c < 1$ is still useful as a conservative bounded-gain constraint for forced simulations, but it is not required for zero-input extinction in the present feed-forward finite graph. With the reservoir wetting update, boundedness follows instead from the projection operator $\Pi_{[0,1]}$ and from the positive drainage term; hence the reservoir component is interpreted as retained wetting storage rather than as a finite-time-extinguishing signal.*

4.3 Boundary conditions and surface forcing

The root node v_0 is driven directly by the scalar forcing signal $f^{(t)}$:

$$\mathbf{x}_{v_0}^{(t)} = \big(f^{(t)},\ f^{(t)},\ \rho_e f^{(t)}\big), \tag{13}$$

where $\rho_e \in [0, 1]$ controls the relative amplitude assigned to the surface erosion-propensity component. All other nodes satisfy $\mathbf{x}_v^{(0)} = \mathbf{0}$ (initially dry, unstressed, undamaged).

Synthetic forcings We consider five canonical forcing types applied at the root, listed in Table 1.

Table 1: Synthetic root forcing scenarios used in the experiments.

Name	Definition	Physical interpretation
Impulse	$A\,\delta_{t,t_0}$	flash flood
Step	$A\,\mathbf{1}_{t\geq t_0}$	groundwater rise
Ramp	$s\,(t-t_0)_+$	seasonal loading
Sinusoid	$A\,[\sin(2\pi t/T_p)]_+$	annual rainfall cycle
Gaussian	$A\,\exp\!\big(-\frac{(t-t_0)^2}{2\sigma^2}\big)$	single storm

4.4 Pressure-threshold exceedance ratio

The main threshold-based risk indicator used in the experiments is not the instantaneous erosion-propensity component $e_v^{(t)}$, but the pore-pressure exceedance of the critical threshold $\tau_{c,v}$. We retain the notation $\mathcal{C}(v)$ for compactness and define it as follows.

Definition 4.4 (Pressure-to-threshold exceedance ratio)**.** *For each node v, define*

$$\mathcal{C}(v) = \max_{0\leq t\leq T} \frac{p_v^{(t)}}{\tau_{c,v}}. \tag{14}$$

A value $\mathcal{C}(v) \geq 1$ means that the pressure threshold is exceeded at least once during the simulation; a value $\mathcal{C}(v) < 1$ means that the node remains below threshold throughout the simulation.

This quantity should be interpreted as a synthetic pressure-threshold hazard indicator. It is not, by itself, a calibrated cumulative internal-erosion law; a physically persistent damage variable would require an additional evolution law driven by the positive part of $p_v^{(t)} - \tau_{c,v}$. Consistently with this interpretation, the implementation uses $p_v^{(t)} > \tau_{c,v}$ for threshold activation metrics, while $e_v^{(t)}$ is retained only as an erosion-propensity proxy. This distinction is not only terminological: in the Gaussian reference case, pressure-threshold activation reaches 32 nodes, whereas thresholding the erosion-propensity component itself would not activate any node, because $e_v^{(t)}$ is not defined as an accumulated damage variable driven by $p_v^{(t)} - \tau_{c,v}$.

4.5 Parametric uncertainty and Monte Carlo propagation

Geotechnical parameters are estimated with uncertainty, as reported in global datasets [PDSB+21, GPL+22]. We model this via:

$$\phi_v \sim \mathcal{N}\big(\mu_v^{\phi},\, (\sigma_{\phi}^{\mathrm{frac}}\,\mu_v^{\phi})^2\big) \cap (0,1), \tag{15}$$

$$\log_{10}\kappa_v \sim \mathcal{N}\big(\log_{10}\mu_v^{\kappa},\, (\sigma_{\kappa}^{\log})^2\big), \tag{16}$$

where $\sigma_{\phi}^{\mathrm{frac}}$ controls the relative uncertainty on porosity and $\sigma_{\kappa}^{\log}$ controls the uncertainty in log-conductivity. The use of a log-scale perturbation for κ_v reflects the fact that hydraulic conductivity may vary over orders of magnitude across soil types. The numerical values used in the experiments are reported in Sect. 5. For each Monte Carlo draw, the recurrence

coefficients induced by the sampled properties are recomputed and the simulation is re-run, while the graph topology and the reference threshold calibration remain fixed. After M runs, mean, standard deviation, and 5th-95th percentile bands are reported for the selected output metrics.

4.6 Output metrics

For a simulation with states $\{\mathbf{x}_v^{(t)}\}$ we compute the following metrics:

First pressure-exceedance time. $t_v^* = \min\{t : p_v^{(t)} > \tau_{c,v}\}$, left undefined if no exceedance occurs within the simulation window.

Pressure-to-threshold exceedance ratio. $\mathcal{C}(v) = P_v^{\max}/\tau_{c,v}$, where $P_v^{\max} = \max_t p_v^{(t)}$.

Nodes activated over time. $n_{\text{act}}(t) = |\{v : p_v^{(t)} > \tau_{c,v}\}|$.

Wetting front depth. $k_\theta(t) = \max\{k : \exists\, v \in V_k,\ \theta_v^{(t)} > \varepsilon_\theta\}$, where $\varepsilon_\theta = q_\theta \max_{v,t} \theta_v^{(t)}$ and q_θ is a relative wetting-front threshold. For HYDRUS-1D comparison, we use the cumulative front $k_\theta^{\text{cum}}(t) = \max_{s \le t} k_\theta(s)$, which is more consistent with a persistent water-content front than an instantaneous pressure pulse.

Cumulative erosion-propensity proxy. $E_v^{\text{cum}} = \sum_{t=0}^{T} e_v^{(t)}$.

5 Experiments

We evaluate the reduced-order model under synthetic surface forcing, nominal Gaussian-threshold calibration, and Monte Carlo perturbations of the geotechnical parameters.

5.1 Setup

All experiments use a graph with $L = 7$ levels ($k = 0, \dots, 6$, 33 nodes total) and $T = 40$ time steps. The Gaussian forcing uses $t_0 = 20$, $A = 2.5$, $\sigma = 5.0$. Unless otherwise stated, the coefficient map in Eq. (12) is instantiated with

$$\begin{aligned} c_0 = 0.35, \qquad c_\kappa = 0.30, \qquad c_\phi = 0.40, \\ b_{\min} = 0.05, \qquad b_{\max} = 0.65, \\ \boldsymbol{\eta}_\alpha = (0.95,\, 1.00,\, 0.80), \qquad \boldsymbol{\eta}_\beta = (0.40,\, 0.35,\, 0.30). \end{aligned} \tag{17}$$

These values are experimental modelling choices used consistently across the synthetic scenarios. The baseline c_0 gives a nonzero propagation level even in poorly conductive zones; c_κ increases propagation as hydraulic conductivity increases; c_ϕ damps propagation in more porous zones to mimic storage; $b_{\min}$ and $b_{\max}$ prevent respectively vanishing and overly large base coefficients. The component weights make the pressure component the reference response, slightly reduce the wetting and erosion-propensity components, and assign lower weight to the secondary $n - 2$ memory term. For the root forcing we set $\rho_e = 0.5$, so

that the erosion-propensity component receives half of the imposed surface signal. For the wetting-front metric we set $q_\theta = 0.01$.

Pressure thresholds $\tau_{c,v}$ are set by normalisation against a reference Gaussian run with nominal parameters. For each node, let $p^{\max,\mathrm{ref}}_{\ell(v)}$ denote the median peak pressure among nodes at the same level as v in the reference run. We define

$$\tau_{c,v} = p^{\max,\mathrm{ref}}_{\ell(v)} \left[\lambda_{\min} + (\lambda_{\max} - \lambda_{\min})\,(1 - \kappa_v^{\mathrm{norm}})\right]. \tag{18}$$

In the experiments we use $\lambda_{\min} = 0.4$ and $\lambda_{\max} = 0.8$. These values define a synthetic threshold range between 40% and 80% of the level-reference peak pressure and are chosen to produce a non-trivial range of sub-threshold and super-threshold responses across the graph. The same threshold field is then kept fixed for all forcing scenarios. This choice is significant because a forcing-dependent recalibration of $\tau_{c,v}$ would make activation counts depend on the chosen reference forcing rather than only on the imposed surface load. This normalisation therefore provides a common synthetic pressure scale for comparing forcing types. Because $\tau_{c,v}$ is derived from a model-generated reference run, the resulting exceedance statistics are interpreted as relative scenario indicators for the synthetic forcing comparison. The Monte Carlo analysis uses $M = 200$ runs. For the Monte Carlo perturbations we set $\sigma_\phi^{\mathrm{frac}} = 0.10$ and $\sigma_\kappa^{\log} = 0.30$. These values define a moderate synthetic uncertainty level for the present numerical study.

5.2 Forcing comparison

Fig. 1 shows the exceedance-ratio map, wetting front, and activated-node count for each of the five forcing types. Table 2 summarises the key scalar metrics.

The impulse forcing produces the fastest but most localised activation: pore pressure spikes at shallow levels and decays rapidly with depth, activating only 5 nodes at peak. As expected from the feed-forward structure in Proposition 4.2, an impulse applied at $t = 5$ vanishes in finite time, with the last nonzero response occurring successively from $t = 5$ at the surface to $t = 11$ at level 6. The step forcing is the mildest in pressure-exceedance terms: despite the sustained loading, the constant amplitude of $A = 0.6$ is too low to overcome the calibrated thresholds, leaving the wetting front at level 0 and activating no node. The ramp forcing, a linearly growing load, propagates through the graph but, under the fixed Gaussian-based thresholds, activates 11 nodes at peak rather than the whole graph. The sinusoid forcing produces periodic activation cycles, with the wetting front oscillating between levels 2 and 5, and only one node active at peak. The Gaussian forcing, resembling a single storm event, shows a smooth bell-shaped activation profile peaking near $t = 22$, with 32 activated nodes. The nonzero values of E^{cum} should be interpreted as cumulative values of the erosion-propensity proxy, not as calibrated physical damage.

5.3 Geomorphological cross-section

To support geophysical interpretation, Fig. 2 shows a *geomorphological cross-section* of the Fibonacci tree under Gaussian forcing. We represent each depth level as a horizontal soil stratum with a natural earth-tone palette (topsoil to bedrock), with node width proportional

Table 2: Summary metrics for the five synthetic forcing scenarios ($L = 7$ levels, $T = 40$, $M_{\text{nodes}} = 33$). $n_{\text{act}}^{\max}$: peak number of simultaneously activated nodes. E^{cum}: total cumulative erosion-propensity proxy $\sum_v E_v^{\text{cum}}$. t_{peak}: time step of peak activation.

Forcing type	$n_{\text{act}}^{\max}$	E^{cum}	t_{peak}
Impulse	5	2.051	9
Step	0	17.931	-
Ramp	11	30.643	39
Sinusoid	1	12.951	8
Gaussian	32	32.130	22

to the number of soil zones at that level (F_{k+1}) and node colour indicating the normalised pore pressure $p_v^{(t)}/\tau_{c,v}$ at the time of peak surface forcing ($t = t_0 = 20$). Nodes with $\mathcal{C}(v) \geq 1$ (pressure threshold exceeded at any time) are outlined in red.

Several features of the propagation are immediately visible. First, the surface levels (0-1) show the highest exceedance-ratio values, reflecting the direct application of forcing at the root. Second, the two deepest levels (5-6) show a mixed pattern: most nodes are at intermediate values ($\mathcal{C} \approx 0.5$-1.2), while a few nodes retain larger inherited pressure signals. Since the edge weights are normalised, this pattern should be interpreted as relative redistribution of the incoming signal rather than as an absolute low-conductivity barrier effect. Third, the strongest pressure localisation occurs where the synthetic conductivity field induces unequal relative partitioning between incoming paths. This is qualitatively compatible with the larger idea that material contrasts can favour preferential erosion initiation at layer boundaries, although the present normalised-weight formulation should not be interpreted as a calibrated model of that mechanism [BFRS03, Fel07]. This visualisation makes the spatial heterogeneity of the propagation front immediately legible in terms of familiar soil stratigraphy.

5.4 Monte Carlo uncertainty band

Fig. 3 reports the 5th-95th percentile bands for wetting front depth and number of activated nodes across 200 Monte Carlo realisations of the geotechnical parameters under Gaussian forcing. The wetting front shows moderate uncertainty in timing but consistent peak depth (5.92 ± 0.26 at the mean peak time, coefficient of variation $\approx 4.4\%$), suggesting that the imposed feed-forward topology constrains the wetting-front trajectory under coefficient-level perturbations. The peak activated-node count is weakly variable in this implementation (32.32 ± 0.55, CV $\approx 1.7\%$), but it remains a thresholded risk indicator whose value depends on the adopted pressure-threshold calibration. These results are summarised in Table 3.

6 HYDRUS-1D Benchmark on Representative Soil Profiles

The synthetic experiments of Sect. 5 are designed to illustrate the internal behaviour of the Fibonacci graph under controlled root forcings. To complement these recurrence-level tests with

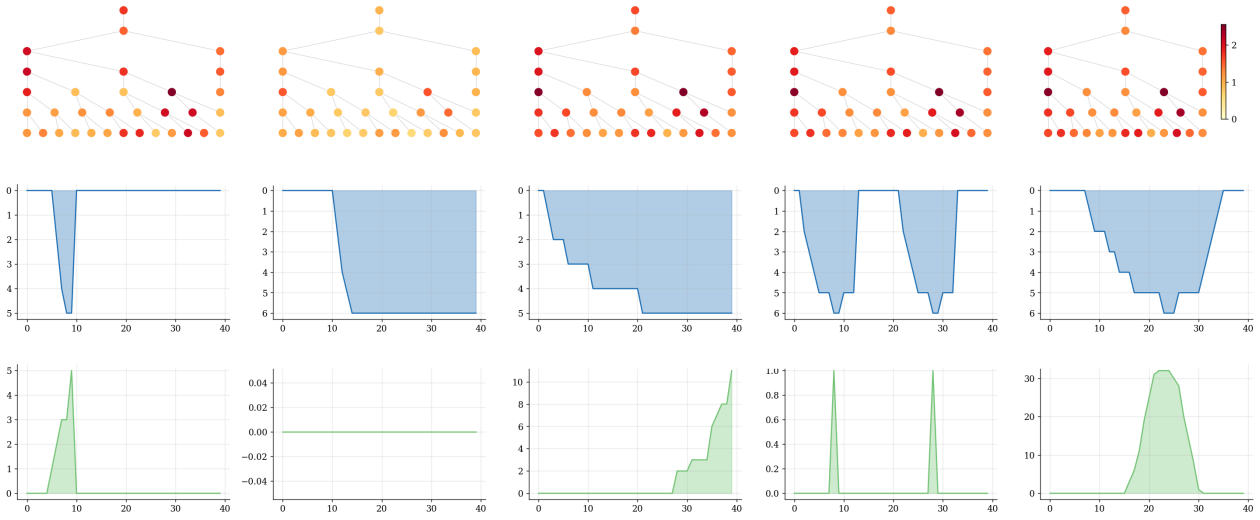

Figure 1: Forcing comparison across five synthetic scenarios: impulse, step, ramp, sinusoid, and Gaussian (from left to right). Top row: pressure-to-threshold exceedance ratio $\mathcal{C}(v)$ on the Fibonacci tree (red indicates $\mathcal{C} > 1$). Middle row: wetting front depth $k_\theta(t)$ (inverted axis, deeper is lower y-axis) over time step t (x-axis). Bottom row: number of activated nodes $n_{\text{act}}(t)$ (y-axis) over time step t (x-axis).

a physically grounded reference, we benchmark the interface-aware reservoir Fibonacci ROM directly against HYDRUS-1D [vvGv08]. HYDRUS-1D solves the one-dimensional Richards equation for variably saturated flow and is widely used as a reference tool for infiltration in layered soils. The goal of this section is to test whether the reduced-order model reproduces the main wetting-front behaviour of a standard Richards-equation solver under comparable hydraulic conditions.

6.1 Benchmark design

We consider two representative van Genuchten–Mualem soil configurations [Mua76, VG80]: a homogeneous sand profile and a layered sand-over-clay profile. The first case tests the ROM response in a highly conductive homogeneous medium; the second case introduces a strong depth-dependent conductivity contrast and is closer to the layered situations that motivate the Fibonacci graph construction. Both profiles are simulated in HYDRUS-1D over a 140 cm vertical domain using an atmospheric upper boundary with surface runoff, free drainage at the bottom, and a Gaussian rainfall event with peak intensity 48 cm/day at $t = 16$ h and standard deviation 4 h. The initial pressure head is set to $h_0 = -200$ cm. The HYDRUS outputs are aggregated onto the same seven depth levels used by the ROM. Table 4 summarises the benchmark setup.

Fig. 4 shows the HYDRUS-1D reference outputs. In the homogeneous sand case, the wetting response propagates rapidly through the profile, as expected from the high saturated conductivity. In the sand-over-clay case, the water-content and pressure-head profiles show a marked change across depth, reflecting the conductivity decrease from the upper sand-rich layers to the deeper clay-rich layers. These two cases therefore provide complemen-

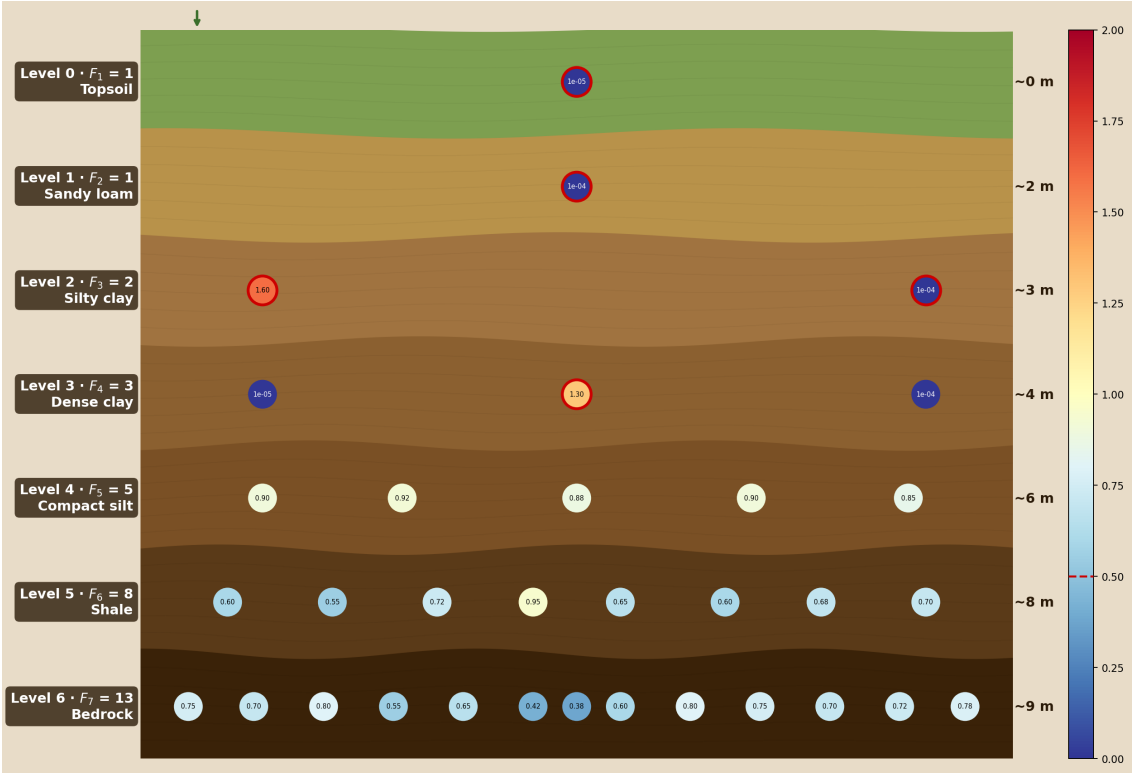

Figure 2: Geomorphological cross-section of the Fibonacci geo-hydraulic graph under Gaussian forcing at $t = t_0 = 20$. Seven strata (Levels 0–6) correspond to Topsoil, Sandy loam, Silty clay, Dense clay, Compact silt, Shale, and Bedrock, with Fibonacci node counts $F_1, \ldots, F_7 = 1, 1, 2, 3, 5, 8, 13$ and approximate depths $0, 2, 3, 4, 6, 8, 9\,\mathrm{m}$ (right margin, $\Delta z \approx 1.5\,\mathrm{m}$ per level). Node colour encodes normalised pore pressure $p_v/\tau_{c,v}$ (blue = safe; red = threshold exceeded); nodes with $\mathcal{C}(v) \geq 1$ are outlined in red. Colorbar range $[0, 2]$; dashed red line marks the pressure threshold.

tary validations on the ROM: fast homogeneous propagation and interface-controlled layered propagation.

6.2 Comparison metrics

For each HYDRUS case, the water-content response is mapped to the same seven-level depth aggregation used by the Fibonacci ROM. Let t_m, $m = 1, \ldots, N_t$, denote the HYDRUS output times, and let $M \in \{\mathrm{H}, \mathrm{F}\}$ indicate either the HYDRUS-1D reference (H) or the Fibonacci ROM (F). We denote by $k_\theta^M(t_m) \in \{0, \ldots, L-1\}$ the aggregated wetting-front depth level predicted by model M at time t_m.

The first metric is the wetting-front trajectory RMSE,

$$\mathrm{RMSE}_{k_\theta} = \left[\frac{1}{N_t} \sum_{m=1}^{N_t} \left(k_\theta^{\mathrm{F}}(t_m) - k_\theta^{\mathrm{H}}(t_m) \right)^2 \right]^{1/2}, \tag{19}$$

which measures the distance between the complete HYDRUS and ROM wetting-front tra-

Table 3: Monte Carlo uncertainty summary ($M = 200$ runs, Gaussian forcing). Nominal simulation statistics are shown alongside the ensemble statistics. CV: coefficient of variation.

Metric (nominal simulation)	Value	-
Total nodes	33	-
Peak activated nodes	32	-
Cumulative erosion $\sum_v E_v^{\mathrm{cum}}$	32.135	-
Exceedance-ratio range $[\min \mathcal{C}, \max \mathcal{C}]$	[0.992, 2.549]	-
Metric (MC ensemble)	**Mean ± Std**	**CV (%)**
Wetting front depth at mean peak time	5.92 ± 0.26	4.4
Peak activated nodes	32.32 ± 0.55	1.7

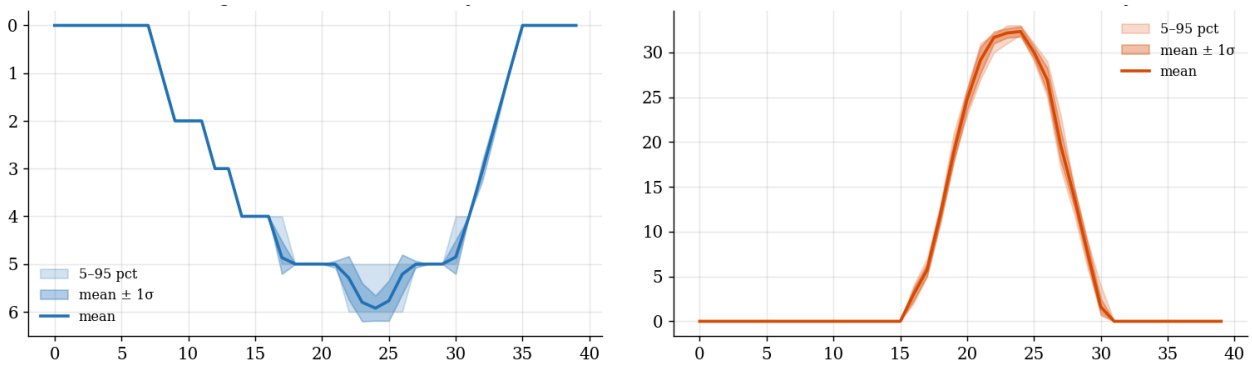

Figure 3: Monte Carlo uncertainty bands ($M = 200$ runs) under Gaussian forcing over time step t ($x-$axis). Left: wetting front depth ($y-$axis) as mean, mean $\pm 1\sigma$, 5-95 % percentile. Right: number of activated nodes ($y-$axis) as same bands over time step t ($x-$axis).

jectories.

The arrival-time error is computed level-wise. For a depth level k, define

$$t_{a,k}^{M} = \min\{t_m : k_\theta^M(t_m) \geq k\}, \qquad M \in \{\mathrm{H}, \mathrm{F}\}, \tag{20}$$

where $t_{a,k}^{M}$ is the first output time at which model M reaches level k. The arrival-time MAE is

$$\mathrm{MAE}_{t_a} = \frac{1}{|\mathcal{K}|} \sum_{k \in \mathcal{K}} \left| t_{a,k}^{\mathrm{F}} - t_{a,k}^{\mathrm{H}} \right|, \tag{21}$$

where $\mathcal{K}$ is the set of depth levels reached by both models within the simulation window.

Peak-depth agreement is measured by the signed peak-depth error

$$\Delta k_{\max} = k_{\max}^{\mathrm{F}} - k_{\max}^{\mathrm{H}}, \qquad k_{\max}^{M} = \max_m k_\theta^M(t_m). \tag{22}$$

Negative values therefore indicate that the ROM reaches a shallower maximum depth than HYDRUS-1D.

Finally, we compare the level-wise attenuation profile. Let $p_k^M(t_m)$ denote the level-aggregated pressure-like response for the ROM or the normalised HYDRUS pressure-head

Table 4: HYDRUS-1D setup used for the controlled benchmark cases.

Item	Value
Domain depth	140 cm
Discretisation	101 nodes, approximately 1.4 cm spacing
Simulation duration	2 days (48 h)
Initial pressure head	$h_0 = -200$ cm
Upper boundary	Atmospheric BC with surface runoff
Lower boundary	Free drainage
Forcing	Gaussian storm, peak 48 cm/day at $t = 16$ h, $\sigma = 4$ h
ROM aggregation	Seven depth levels
ROM variant	Interface-aware reservoir Fibonacci ROM
Interface strength	$s_I = 1.25$

Table 5: Direct HYDRUS-1D benchmark of the interface-aware reservoir Fibonacci ROM under Gaussian storm forcing. Wetting-front errors are computed on the seven-level depth aggregation used by the ROM.

Profile	Wetting-front RMSE RMSE_{k_θ} [levels]	Arrival-time MAE MAE_{t_a} [h]	Peak-depth error $\Delta k_{\max}$ [levels]	Attenuation RMSE RMSE_A [-]	Attenuation corr. r_A [-]
Homogeneous sand	1.273	5.286	0.000	0.216	0.200
Sand-over-clay	0.990	4.428	-1.000	0.779	0.225

response for the reference model. We define

$$A_k^M = \frac{\max_m p_k^M(t_m)}{\max_m p_0^M(t_m)}, \tag{23}$$

and report the attenuation-profile RMSE

$$\mathrm{RMSE}_A = \left[\frac{1}{|\mathcal{K}_A|} \sum_{k \in \mathcal{K}_A} \left(A_k^{\mathrm{F}} - A_k^{\mathrm{H}} \right)^2 \right]^{1/2}, \tag{24}$$

together with the Pearson correlation r_A between the two attenuation vectors. The set $\mathcal{K}_A$ contains the depth levels included in the attenuation comparison. These metrics are reported in Table 5.

Fig. 5 compares the HYDRUS wetting-front trajectories with the Fibonacci ROM. In both benchmark cases the ROM reproduces the main timing and depth progression of the HYDRUS front. The homogeneous sand case has $\mathrm{RMSE}_{k_\theta} = 1.27$ levels and $\mathrm{MAE}_{t_a} = 5.29$ h. The layered sand-over-clay case has $\mathrm{RMSE}_{k_\theta} = 0.99$ levels and $\mathrm{MAE}_{t_a} = 4.43$ h, indicating that the interface-aware correction is effective in the stratified configuration for which it was introduced.

6.3 Interpretation

The HYDRUS-1D benchmarks support the use of the Fibonacci ROM as a rapid screening model. The agreement is strongest for the wetting-front trajectory, which is the quantity most

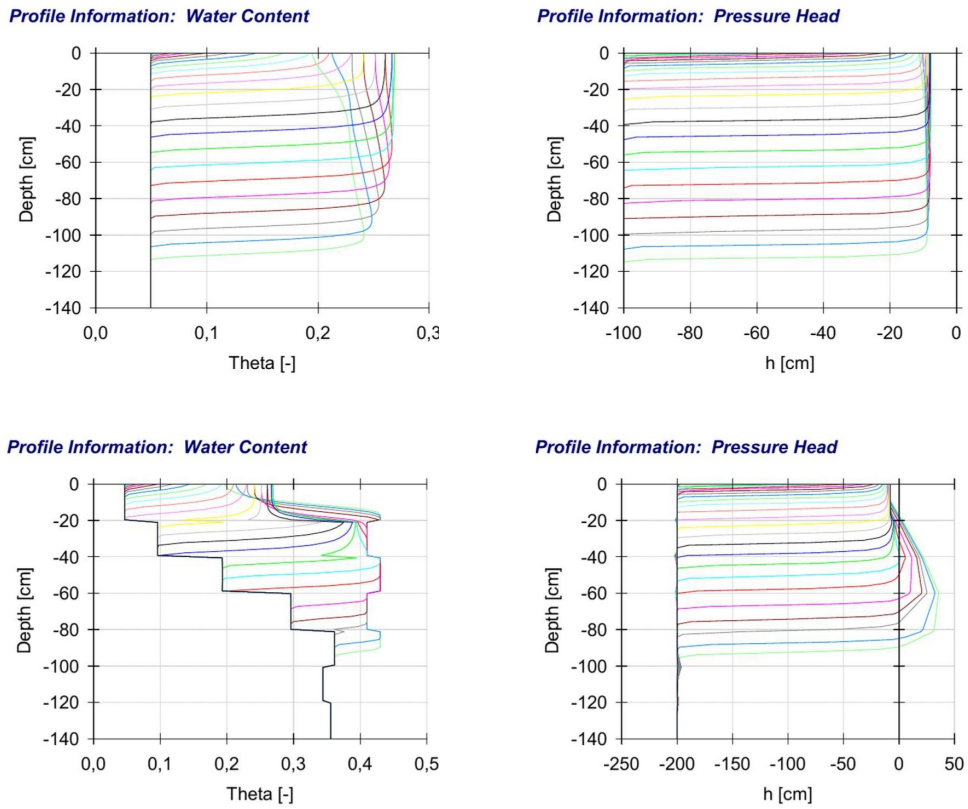

Figure 4: HYDRUS-1D reference simulations for the two benchmark profiles under Gaussian storm forcing. Top row: homogeneous sand. Bottom row: sand-over-clay. Left column: water-content profiles. Right column: pressure-head profiles.

directly comparable between the two models. The attenuation metrics are less favourable, especially in the layered case, because HYDRUS reports pressure head and water-content profiles governed by the nonlinear Richards equation, whereas the ROM propagates a dimensionless pressure-threshold indicator. The benchmark should therefore be interpreted as a controlled solver-based validation of wetting-front behaviour. A natural extension is to perform the same comparison using monitored laboratory columns or field profiles with measured rainfall, soil-water content, and pressure-head time series.

7 Discussion

7.1 Comparison with Richards-equation solvers

Full numerical solvers for the Richards equation (e.g., HYDRUS-1D [vvGv08]) provide the highest physical fidelity for one-dimensional unsaturated flow, reproducing the nonlinear dependence of conductivity and capillary pressure on water content and producing mass-conservative solutions even for sharp wetting fronts [BFRS03]. Their computational cost, however, scales with the spatial discretisation and the number of Newton iterations required for convergence, making them impractical for large Monte Carlo ensembles without surrogate

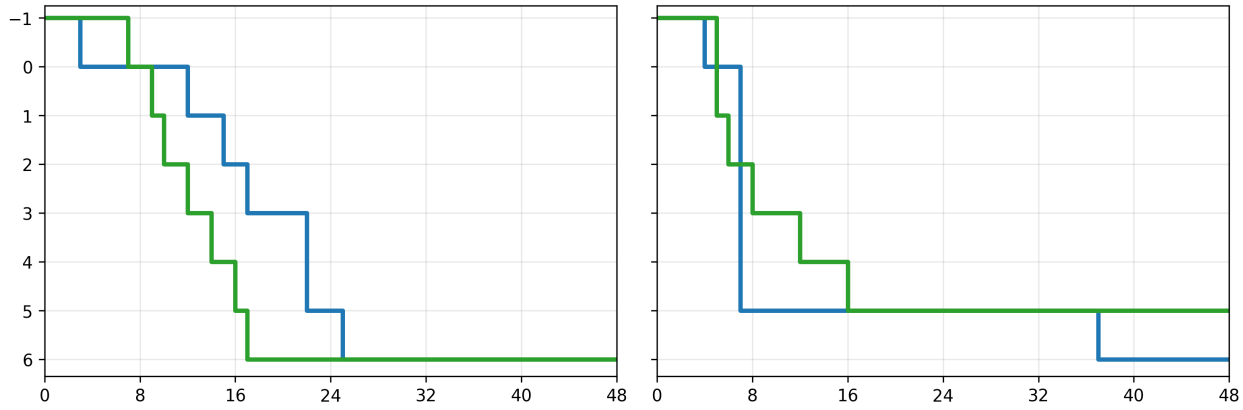

Figure 5: Comparison between HYDRUS-1D and Fibonacci ROM wetting-front trajectories (y-axis) over time (x-axis) for the two benchmark cases: homogeneous sand (left) and sand-over-clay (right). The blue line denotes the HYDRUS-1D reference, while the green line denotes the Fibonacci ROM.

acceleration.

The Fibonacci ROM sacrifices some physical detail: it does not represent hysteresis, it linearises the nonlinear conductivity function through fixed coefficients, and it decouples the three state components, in exchange for closed-form recurrence that can be evaluated in milliseconds. In the experiments of Sect. 5, 200 Monte Carlo runs complete in under one second on a standard laptop. The HYDRUS-1D benchmarks of Sect. 6 provide a controlled external comparison with a standard Richards-equation solver. They show that the interface-aware reservoir Fibonacci ROM captures the HYDRUS wetting-front progression in both a homogeneous sand profile and a sand-over-clay profile, with errors on the order of one depth level. At the same time, the pressure/attenuation comparison remains less direct because the ROM pressure variable is a normalised pressure-threshold indicator rather than a pressure head. The model is therefore best understood as a complement to high-fidelity solvers: it is suited to rapid hazard screening, sensitivity analysis, and parameter importance ranking, while site-specific design would still require a Richards-equation solver calibrated against field data.

7.2 Comparison with dual-porosity models

Dual-porosity models [GVG93] explicitly represent the exchange between mobile (macropore) and immobile (matrix) domains, producing breakthrough curves that exhibit early arrival of tracers and long tailing. This structure is particularly important for soils with well-developed macroporosity or for contaminant transport. The Fibonacci graph can be interpreted as a multi-rate extension of the dual-porosity concept: the primary parent connection ($n-1$ memory) and secondary parent connection ($n-2$ memory) act as two pathways with different effective conductivities. However, the model does not include an explicit mobile-immobile mass transfer coefficient, so it cannot reproduce the tailing behaviour characteristic of dual-porosity systems. Further extensions could introduce such a term as an additional coupling between the θ and p components of adjacent nodes.

7.3 Comparison with pore-network models

Pore-network models [KPRAM23, TZBL21] resolve individual pore throats and explicitly represent pore-size distributions, providing mechanistic predictions of permeability, capillary entry pressure, and grain-scale erosion. They are complementary to continuum models at the opposite end of the scale spectrum. The Fibonacci graph operates at the scale of soil zones (decimetres to metres), where individual pore geometry is not resolved; it is closer in spirit to continuum models. The main distinguishing feature is the prescribed, aperiodic branching topology, which is not derived from a pore-space image but imposed as a modelling hypothesis about the structure of preferential pathways.

7.4 Topological ablation: why Fibonacci?

A natural question is whether the Fibonacci branching rule is actually necessary, or whether a simpler topology would produce equivalent results at lower complexity. To address this, we compare three graph topologies at equal depth ($L = 7$ levels, $T = 60$ time steps, seed $= 42$): the *Chain* (one node per level, pure 1-D column with only $n-1$ memory), the *Binary Tree* (2^k nodes at level k, $n-1$ memory only), and the *Fibonacci* graph as defined in Sect. 3. All three share the same geotechnical property distributions, the same random seed (ensuring matched node properties at corresponding levels), and the same simulator logic. Three forcing types are tested (Gaussian, impulse, step); here we focus on Gaussian, which is the most physically representative of a single storm event.

Node counts and computational cost The three topologies span a wide range of complexity at equal depth: Chain has 7 nodes, Fibonacci has 33, and Binary Tree has 127. In terms of node-timestep operations (the principal cost proxy), Fibonacci is 4.7× more expensive than Chain and 3.8× cheaper than Binary Tree (Table 6).

Quantitative comparison Table 6 reports the key metrics under Gaussian forcing. Two results stand out. First, the *wetting front arrival at the deepest level*: Chain never reaches depth $k = 6$ within $T = 60$ steps (arrival = 60, i.e. never), while both Fibonacci and Binary Tree arrive at step $t = 23$. This means that the pure 1-D column model, despite its simplicity, fails to reproduce deep penetration dynamics within the simulation window, a result consistent across the tested synthetic setting, suggesting that branching and recurrence-memory structure are descriptively important rather than cosmetic. Note that all three topologies activate a comparable *fraction* of their available nodes under Gaussian forcing (100%, 94%, and 97% for Chain, Binary Tree, and Fibonacci respectively), so the absolute peak counts in Table 6 reflect node-count differences rather than qualitative differences in exceedance behaviour. Second, the *signal attenuation ratio* at the deepest level: Fibonacci reaches 0.0074 against 0.0134 (Chain) and 0.0128 (Binary Tree). Within this synthetic model, the lower attenuation ratio of Fibonacci is a consequence of the dual-memory recurrence ($n-1$ and $n-2$ parents), which redistributes the incoming signal over two ancestral levels. Chain and Binary Tree, both operating with $n-1$ memory only, produce nearly identical attenuation profiles despite their very different node counts.

Table 6: Topological ablation study: key metrics under Gaussian forcing ($L = 7$ levels, $T = 60$, seed $= 42$).

Metric	Chain	Binary Tree	Fibonacci
Total nodes	7	127	33
Node-step operations (rel.)	1.0×	18.1×	4.7×
Peak activated nodes	7	119	32
Fraction of activated nodes	100%	94%	97%
Propagation delay (steps)	6.00	6.00	4.08
Signal attenuation ratio (level 6)	0.0134	0.0128	0.0074
Structural entropy H	1.277	1.781	1.642
Wetting front: arrival at $k = 6$	60	23	23
Depth-level attenuation profile (normalised mean peak pressure)			
Level 0	1.00000	1.00000	1.00000
Level 1	0.42666	0.46961	0.42666
Level 2	0.21869	0.23379	0.17450
Level 3	0.10305	0.11379	0.08922
Level 4	0.05395	0.05428	0.03943
Level 5	0.02733	0.02639	0.01726
Level 6	0.01339	0.01280	0.00742

Structural entropy and spatial heterogeneity We compute the Shannon entropy of the exceedance-ratio distribution as a scalar measure of spatial heterogeneity in the synthetic risk pattern. This entropy is higher for Fibonacci ($H = 1.64$) and Binary Tree ($H = 1.78$) than for Chain ($H = 1.28$). A higher H indicates that the model resolves a wider spectrum of risk levels across nodes, which is an argument in favour of branching topologies for hazard mapping applications where spatial differentiation of risk is required.

Sensitivity to forcing type Table 7 reports the relative variability of three scalar metrics across the Gaussian, impulse, and step forcing scenarios. For each topology and metric, the table gives the coefficient of variation $CV = 100\,\sigma/|\mu|$, where μ and σ are the mean and standard deviation of that metric over the three forcing cases. The table therefore measures forcing-dependence, not parametric uncertainty. The attenuation ratio is nearly forcing-insensitive for Chain and Binary Tree (CV $\approx 0\%$), while Fibonacci shows a moderate sensitivity in attenuation (CV $= 14\%$), reflecting the richer dynamics introduced by the dual-memory recurrence. Cumulative erosion is uniformly sensitive across all topologies (CV $\approx 64\%$), confirming that it is a forcing-driven quantity rather than a topology-driven one. Because the recurrence is linear in the root-forcing amplitude, changing the Gaussian amplitude rescales the full state trajectory proportionally. Moreover, because the edge weights are normalised, attenuation ratios describe structural redistribution through the recurrence rather than absolute hydraulic dissipation.

Fig. 6 shows the full activation dynamics across all topology-forcing combinations. The contrast between topologies is visually immediate: Chain produces a flat, slow-rising response

Table 7: Relative variability of selected scalar metrics across forcing scenarios. For each topology and metric, the table reports the coefficient of variation $CV = 100\,\sigma/|\mu|$ computed over the Gaussian, impulse, and step forcing cases.

Metric	Chain	Binary Tree	Fibonacci
Peak activated	56.6%	28.6%	32.6%
Cumulative erosion	64.1%	64.1%	64.1%
Attenuation ratio	0.0%	0.0%	14.0%

dominated by the single propagation path; Binary Tree reaches large absolute counts in short bursts, reflecting the exponential node growth at deep levels; Fibonacci sustains a broader and temporally smoother activation profile, a direct consequence of the dual-memory recurrence distributing energy across a wider time window.

Summary Fig. 7 shows the wetting front time series for all three topologies, and Fig. 8 shows the depth-level attenuation profiles. The two figures together make the key trade-off visible: Chain is the cheapest but fails to capture deep penetration; Binary Tree captures deep penetration but at 18× the cost of Chain and with attenuation dynamics indistinguishable from Chain; Fibonacci captures deep penetration *and* produces a qualitatively richer attenuation profile at only 4.7× the cost of Chain. Among the three topologies tested, Fibonacci provides the most favourable trade-off in the complexity-descriptive capacity space: it achieves the greatest descriptive improvement per unit of additional computational cost.

7.5 Limitations

The main limitations of the present model are the following. First, the recurrence coefficients are derived from a heuristic map of porosity and conductivity (Equation (12)); future work should calibrate these coefficients against additional HYDRUS-1D cases, laboratory column data, or field data for specific soil types, and assess whether the map is identifiable from standard laboratory measurements. Second, the model includes a local reservoir update for the wetting state, but the pressure and erosion-propensity components remain only weakly coupled; it therefore still cannot fully represent capillary suction-driven redistribution, where drying at one depth can draw water upward from wetter zones below, or poroelastic coupling where skeleton deformation modifies pore pressure. Third, the model is strictly one-dimensional in depth and does not represent lateral flow, slope effects, anisotropy, or two-dimensional pressure gradients that govern hillslope stability problems.

8 Conclusions and Future Work

We have introduced the Fibonacci geo-hydraulic propagation model, a reduced-order framework for simulating infiltration and internal erosion in heterogeneous layered soils. The model encodes the branching structure of subsurface preferential pathways as a Fibonacci graph, propagates wetting signal, pore pressure, and an erosion-propensity proxy via a Fibonacci-like

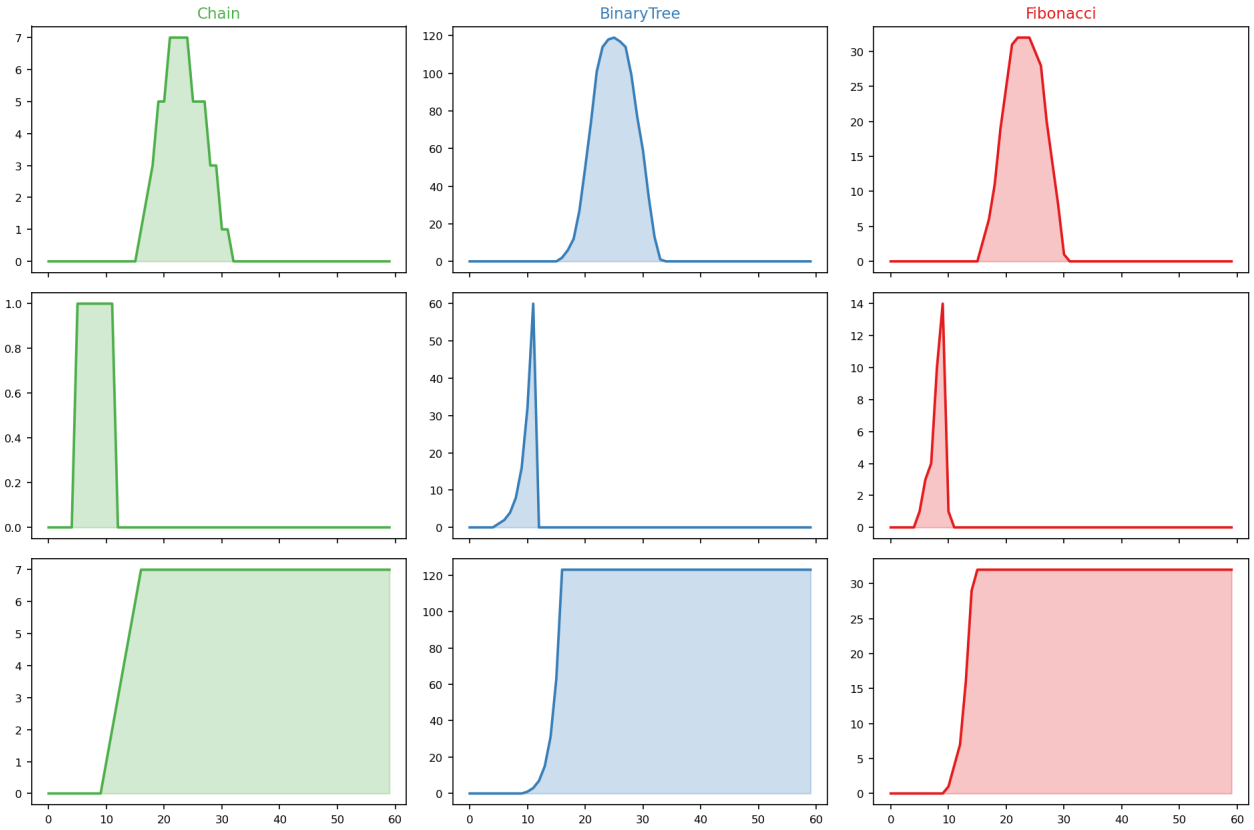

Figure 6: Number of activated nodes (y-axis) over time step t (x-axis) for all three topologies (columns: Chain, Binary Tree, Fibonacci) under three forcing types (rows: Gaussian, impulse, step).

recurrence with geotechnically parameterised coefficients, and defines a pressure-to-threshold exceedance ratio to characterise which nodes undergo threshold activation. For wetting-front benchmarking, the model is augmented with a local reservoir state and an interface-aware hydraulic-contrast correction, preserving the Fibonacci graph while improving comparability with Richards-equation simulations.

The experimental results show that the model produces qualitatively interpretable outputs across five canonical forcing scenarios. Under Gaussian forcing (single storm), 32 of 33 nodes are eventually activated with peak pressure-to-threshold ratios up to 2.55. The Monte Carlo analysis indicates that the wetting front depth is weakly sensitive to coefficient-level parameter variability, while activated-node metrics are more strongly affected by thresholding choices and geotechnical uncertainty. All 200 Monte Carlo runs complete in under one second, demonstrating the computational advantage of the recurrence-based approach. The illustrated geomorphological cross-section provides an intuitive representation of the propagation front that connects the abstract graph structure to physical soil stratigraphy. In addition, direct HYDRUS-1D benchmarks on homogeneous sand and sand-over-clay profiles show that the interface-aware reservoir ROM reproduces the HYDRUS wetting-front trajectory with errors on the order of one depth level under the Gaussian storm forcing used here. These results support the use of the model as a rapid screening tool.

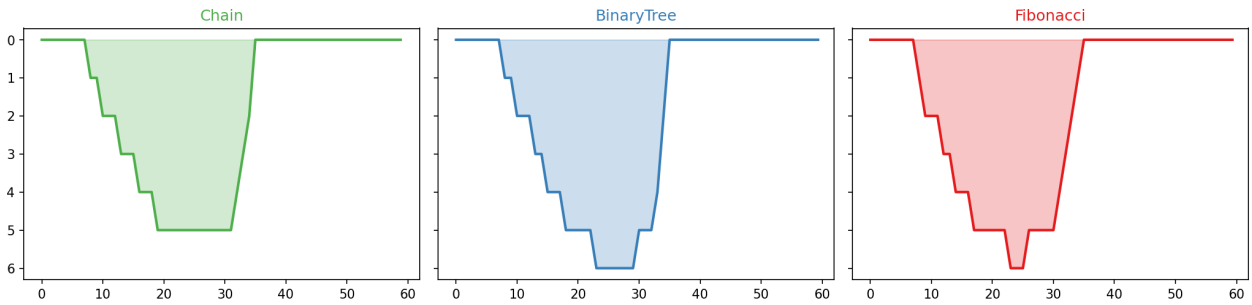

Figure 7: Wetting front depth (y-axis) over time step t (x-axis) for Chain (left), Binary Tree (centre), and Fibonacci (right) under Gaussian forcing.

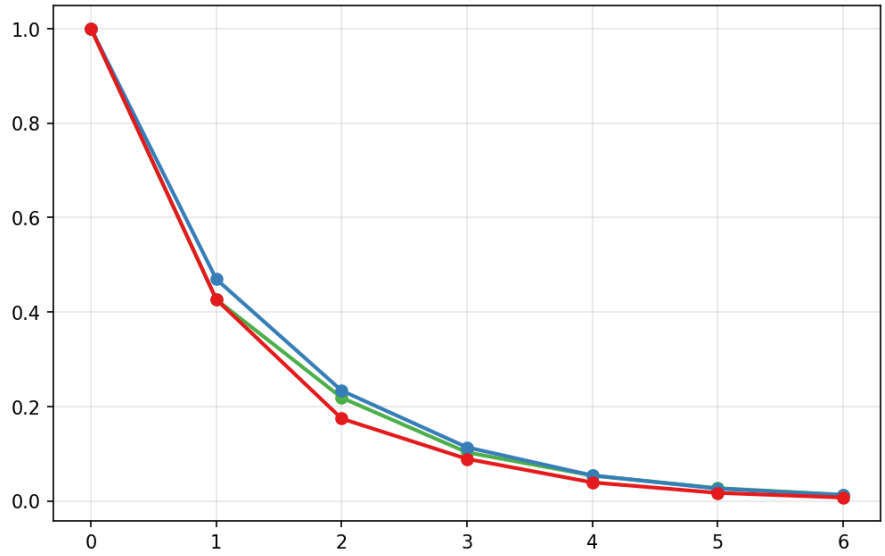

Figure 8: Depth-level signal attenuation profile under Gaussian forcing. Mean peak pressure normalised to the root peak (y-axis), at each depth level (x-axis): Fibonacci (red line), Chain (green line), and Binary Tree (blue line).

Future work Several extensions are identified.

(i) **Extension of HYDRUS-1D benchmarking and calibration.** The present HYDRUS-1D comparison covers two representative Gaussian-storm cases. A systematic extension across additional USDA texture classes, layered profiles, rainfall histories, and initial moisture states would establish the range of conditions under which the ROM remains accurate and would identify the coefficient and reservoir-interface parameters that minimise the discrepancy.

(ii) **Poroelastic coupling.** Including the stiffness modulus E_v in the recurrence would allow the model to represent skeleton deformation and its feedback on pore pressure, moving toward a Biot-like coupled formulation.

(iii) **Real-data validation.** Application to monitored embankment dams, laboratory infiltration columns, or instrumented slopes with measured rainfall, water-content,

pressure-head, and seepage-response records would provide the first quantitative test of the model against field observations.

(iv) **Extension to two dimensions.** A two-dimensional version of the graph, with lateral as well as vertical connections, would allow the model to represent slope processes, lateral drainage, and two-dimensional pressure gradients relevant to levee and embankment dam safety assessment.

A Notation summary

Symbol	Meaning	Unit / Range
$\mathcal{T} = (V, E, W)$	Fibonacci geo-hydraulic graph	-
V_k	nodes at depth level k	$\lvert V_k \rvert = F_{k+1}$
L	number of depth levels	$\mathbb{N}$
$p_1(v), p_2(v)$	primary / secondary parent	V_{k-1}, V_{k-2}
ϕ_v	porosity	$(0, 1)$
κ_v	saturated hydraulic conductivity	m s^{-1}
E_v	drained stiffness modulus	MPa
$\tau_{c,v}$	pressure threshold	normalised
$w_{u \to v}$	unnormalised edge weight	m s^{-1}
$\tilde{w}_1, \tilde{w}_2$	normalised edge weights	$[0, 1]$
$\mathbf{x}_v^{(t)}$	state vector (θ, p, e)	$\mathbb{R}^3$
α_v, β_v	recurrence coefficient vectors	$\mathbb{R}^3$
b_v	base propagation coefficient	$(b_{\min}, b_{\max})$
c_0, c_κ, c_ϕ	coefficient-map parameters	synthetic
$\boldsymbol{\eta}_\alpha, \boldsymbol{\eta}_\beta$	component multipliers	$\mathbb{R}^3_+$
ρ_e	root erosion-propensity forcing fraction	$[0, 1]$
$\lambda_{\min}, \lambda_{\max}$	threshold normalisation fractions	$[0, 1]$
q_θ	relative wetting-front threshold	$[0, 1]$
$\sigma_\phi^{\text{frac}}, \sigma_\kappa^{\log}$	MC uncertainty parameters	synthetic
$\mathbf{f}_v^{(t)}$	external forcing	$\mathbb{R}^3$
$\mathcal{C}(v)$	pressure-to-threshold exceedance ratio	$\mathbb{R}_{\geq 0}$
t_v^*	first pressure-exceedance time	$\{0, \ldots, T\}$ or undefined
$n_{\text{act}}(t)$	activated nodes at time t	$\mathbb{N}$
$k_\theta(t)$	wetting front depth	$\{0, \ldots, L-1\}$

Acknowledgements

SC is part of RAISE Innovation Ecosystem, funded by the European Union, NextGenerationEU and by the Ministry of University and Research (MUR), National Recovery and Resilience Plan, Mission 4, Component 2, Investment 1.5, project "RAISE, Robotics and AI for Socio-economic Empowerment" (ECS00000035).

References

[BFRS03] B. Brunone, M. Ferrante, N. Romano, and A. Santini. Numerical simulations of one-dimensional infiltration into layered soils with the Richards equation using different estimates of the interlayer conductivity. *Vadose Zone Journal*, 2:193–200, 2003.

[BGW15] P. Benner, S. Gugercin, and K. Willcox. A survey of projection-based model reduction methods for parametric dynamical systems. *SIAM Review*, 57:483–531, 2015.

[Bio41] M. A. Biot. General theory of three-dimensional consolidation. *Journal of Applied Physics*, 12:155–164, 1941.

[Dar56] Henry Darcy. *Les fontaines publiques de la ville de Dijon: Exposition et application des principes à suivre et des formules à employer dans les questions de distribution d'eau: Ouvrage terminé par un appendice relatif aux fournitures d'eau de plusieurs villes, au filtrage des eaux et à la fabrication des tuyaux de fonte, de plomb, de tôle et de bitume*, volume 2. Victor Dalmont, éditeur, 1856.

[DC12] L. J. Durlofsky and Y. Chen. Uncertainty quantification for subsurface flow problems using coarse-scale models. In I. G. Graham, T. Y. Hou, O. Lakkis, and R. Scheichl, editors, *Numerical Analysis of Multiscale Problems*, volume 83 of *Lecture Notes in Computational Science and Engineering*, pages 163–202. Springer, Berlin, Heidelberg, 2012.

[DYCW22] Sirui Deng, Haoqing Yang, Xiaoying Chen, and Xin Wei. Probabilistic analysis of land subsidence due to pumping by biot poroelasticity and random field theory. *Journal of Engineering and Applied Science*, 69(1):18, 2022.

[Fel07] R. Fell. The mechanics of internal erosion and piping of embankment dams and their foundations. In *Proceedings of the 10th Australia–New Zealand Conference on Geomechanics*, Brisbane, 2007.

[FF07] Robin Fell and Jean-Jacques Fry. *Internal erosion of dams and their foundations: selected and reviewed papers from the workshop on internal erosion and piping of dams and their foundations, Aussois, France, 25–27 April 2005*. Crc Press, 2007.

[FO17] Matthew W Farthing and Fred L Ogden. Numerical solution of richards' equation: A review of advances and challenges. *Soil Science Society of America Journal*, 81(6):1257–1269, 2017.

[GPL+22] Surya Gupta, Andreas Papritz, Peter Lehmann, Tomislav Hengl, Sara Bonetti, and Dani Or. Global soil hydraulic properties dataset based on legacy site observations and robust parameterization. *Scientific Data*, 9(1):444, 2022.

[GVG93] H. H. Gerke and M. Th. Van Genuchten. A dual-porosity model for simulating the preferential movement of water and solutes in structured porous media. *Water Resources Research*, 29:305–319, 1993.

[HLP14] O. Hungr, S. Leroueil, and L. Picarelli. The Varnes classification of landslide types, an update. *Landslides*, 11:167–194, 2014.

[Jia24] Jiamin Jiang. Simulating multiphase flow in fractured media with graph neural networks. *Physics of Fluids*, 36(2), 2024.

[KM03] Dan Kalman and Robert Mena. The fibonacci numbers—exposed. *Mathematics magazine*, 76(3):167–181, 2003.

[KPRAM23] Z. Kanavas, F. J. Pérez-Reche, F. Arns, and V. L. Morales. Flow path resistance in heterogeneous porous media recast into a graph-theory problem. *Transport in Porous Media*, 146:267–282, 2023.

[Leh30] Derrick Henry Lehmer. An extended theory of Lucas' functions. *Annals of Mathematics*, 31(3):419–448, 1930.

[LFOJ23] Peter La Follette, Fred L Ogden, and Ahmad Jan. Layered Green and Ampt infiltration with redistribution. *Water Resources Research*, 59(7):e2022WR033742, 2023.

[LSC14] Wei-Cheng Lo, Garrison Sposito, and Hsiuhua Chu. Poroelastic theory of consolidation in unsaturated soils. *Vadose Zone Journal*, 13(5):vzj2013–07, 2014.

[LSC+25] Feng Liu, Jenisha Singh, Chao Chen, Yang Li, and Gang Wang. Hydrological and mechanical behavior of granular materials subjected to internal erosion: A review. *KSCE Journal of Civil Engineering*, 29(2):100047, 2025.

[LSFW25] Yanling Li, Qianxing Sun, Yuliang Fu, and Junfang Wei. Solving the Richards infiltration equation by coupling physics-informed neural networks with Hydrus-1D. *Scientific Reports*, 15(1):18649, 2025.

[LTL24] L. Liang, D.-L. Tian, and Z.-C. Li. Internal erosion process and its influence factors in widely graded loose soils due to rainfall infiltration. *Frontiers in Earth Science*, 12:1418293, 2024.

[MCP+26] Marianna Miola, Daniela Cabiddu, Simone Pittaluga, Micaela Raviola, and Marino Vetuschi Zuccolini. EWoPe: A light Embeddable WOrkflow PErsistence tool for geoscientific pipeline reproducibility. *Computers & Geosciences*, page 106099, 2026.

[Mua76] Y. Mualem. A new model for predicting the hydraulic conductivity of unsaturated porous media. *Water Resources Research*, 12:513–522, 1976.

[NKE19] J. Nagoor Kani and A. H. Elsheikh. Reduced-order modeling of subsurface multi-phase flow models using deep residual recurrent neural networks. *Transport in Porous Media*, 126:713–741, 2019.

[PBBK08] Chan-Hee Park, Christof Beyer, Sebastian Bauer, and Olaf Kolditz. A study of preferential flow in heterogeneous media using random walk particle tracking. *Geosciences Journal*, 12(3):285–297, 2008.

[PDSB+21] Laura Poggio, Luis M De Sousa, Niels H Batjes, Gerard Heuvelink, Bas Kempen, Eloi Ribeiro, and David Rossiter. SoilGrids 2.0: producing soil information for the globe with quantified spatial uncertainty. *Soil*, 7(1):217–240, 2021.

[PGP14] D. Pasetto, A. Guadagnini, and M. Putti. A reduced-order model for Monte Carlo simulations of stochastic groundwater flow. *Computational Geosciences*, 18:157–169, 2014.

[QMN15] A. Quarteroni, A. Manzoni, and F. Negri. *Reduced Basis Methods for Partial Differential Equations: An Introduction*. Springer, Cham, 2015.

[Ric31] L. A. Richards. Capillary conduction of liquids through porous mediums. *Physics*, 1:318–333, 1931.

[Sah94] M. Sahimi. *Applications of Percolation Theory*. Taylor & Francis, London, 1994.

[Tao18] Hui Tao. *Numerical modeling of soil internal erosion mechanism*. PhD thesis, University of Akron, 2018.

[TPTG17] Alexandre M Tartakovsky, M Panzeri, GD Tartakovsky, and A Guadagnini. Uncertainty quantification in scale-dependent models of flow in porous media. *Water Resources Research*, 53(11):9392–9401, 2017.

[TZBL21] YB Tang, JZ Zhao, Y Bernabé, and M Li. Fluid flow concentration on preferential paths in heterogeneous porous media: application of graph theory. *Journal of Geophysical Research: Solid Earth*, 126(12):e2021JB023164, 2021.

[VG80] M. Th. Van Genuchten. A closed-form equation for predicting the hydraulic conductivity of unsaturated soils. *Soil science society of America journal*, 44(5):892–898, 1980.

[vvGv08] J. Šimůnek, M. T. van Genuchten, and M. Šejna. Development and applications of the HYDRUS and STANMOD software packages and related codes. *Vadose Zone Journal*, 7:587–600, 2008.

[ZLEB21] E. Zehe, R. Loritz, Y. Edery, and B. Berkowitz. Preferential pathways for fluid and solutes in heterogeneous groundwater systems: self-organization, entropy, work. *Hydrology and Earth System Sciences*, 25:5337–5353, 2021.